PAPER

Check for updates

Highly sensitive detection of *Salmonella typhimurium via* gold and magnetic nanoparticle-mediated sandwich hybridization coupled with ICP-MS†

Yujie Zhou, [a] Zhihui Tang, [b] Lei Li, [a] Yuzuo Chen, [b] Yuanyuan Xu, [a] Renjie Liu, [b] Yanrong Zhang, [b] Xiaoyan Liu, [c] Wenjuan Yang, [d] Baoning Wang, [b] Jieyu Zhang, *[a] Qing Jiang*[a] and Yunbing Wang [a]

Foodborne pathogens including *Salmonella typhimurium* (*S. typhimurium*) are responsible for over 600 million global incidences of illness annually, posing a significant threat to public health. Inductively coupled plasma mass spectrometry (ICP-MS), coupled with element labeling strategies, has emerged as a promising platform for multivariate and accurate pathogen detection. However, achieving high specificity and sensitivity remains a critical challenge. Herein, we synthesize clustered magnetic nanoparticles (MNPs) and popcorn-shaped gold nanoparticles (AuNPs) to conjugate capture and report DNA probes for *S. typhimurium*, respectively. These engineered nanoparticles facilitate the identification of *S. typhimurium* DNA through a sandwich hybridization technique. ICP-MS quantification of Au within the sandwich-structure complexes allows for precise *S. typhimurium* detection. The unique morphology of the AuNPs and MNPs increases the available sites for probe attachment, enhancing the efficiency of *S. typhimurium* DNA capture, broadening the detection range to 10^1–10^{10} copies mL^{-1}, and achieving a low detection limit of 1 copy mL^{-1}, and the overall assay time is 70 min. The high specificity of this method is verified by anti-interference assays against ten other pathogens. The recovery was 96.8–102.8% for detecting *S. typhimurium* DNA in biological samples. As these specially designed nanoparticles may facilitate the attachment of various proteins and nucleic acid probes, they may become an effective platform for detecting multiple pathogens.

[a] National Engineering Research Center for Biomaterials, Sichuan University, Chengdu, Sichuan, 610065, China. E-mail: jieyu@scu.edu.cn, jiangq@scu.edu.cn; Fax: +86 028 85410246; Tel: +86 028 85410537

[b] West China School of Basic Medical Sciences and Forensic Medicine, Sichuan University, Chengdu, Sichuan, 610041, China

[c] Department of Orthopedic Surgery, West China Hospital, Sichuan University/West China School of Nursing, Chengdu, Sichuan, 610041, China

[d] Department of Gastroenterology, West China Hospital, Sichuan University, Chengdu, Sichuan, 610041, China

† Electronic supplementary information (ESI) available. See DOI: https://doi.org/10.1039/d4tb00291a

1. Introduction

The World Health Organization has identified foodborne illness as an escalating global issue, with over 600 million cases annually, mainly caused by pathogen-contaminated food.[1] *Salmonella typhimurium* (*S. typhimurium*) is a major contributor to foodborne illness and a significant health hazard.[2] The Centers for Disease Control and Prevention highlighted that *S. typhimurium* infections cause about 450 deaths and 23 000 hospitalizations each year in the USA, with associated direct medical costs amounting to $365 million.[3] Therefore, the development of rapid, sensitive, and reliable strategies for *S. typhimurium* detection is critical to enhancing food safety, reducing the risk of infections, and guiding the timely clinical response alongside effective pharmacological interventions.

Current methods for *S. typhimurium* detection mainly include the traditional plate culture method,[4] enzyme-linked immunosorbent assays,[5,6] and polymerase chain reaction.[7–10] Despite their widespread adoption, these methods suffer from disadvantages, such as being time-consuming,[11] and in certain contexts, compromised accuracy.[12] Consequently, there is an imperative need to construct more convenient, easy-to-operate, and accurate detection methods for *S. typhimurium* detection. Recent advancements have led to the development of new biosensors, including optical and electrochemical biosensors,[13–17] which involve quantum dots[18–21] and lanthanide metals[22,23] and offer advantages of fast response, ease of use, and good sensitivity.[2] However, these new methods are not without limitations. For example, the color change or colorimetric signals of optical biosensors are easily interfered with by impurities in the sample,[22] and most electrochemical biosensors rely on labeled

This journal is © The Royal Society of Chemistry 2024

J. Mater. Chem. B, 2024, **12**, 7311–7323 | **7311**

probes or complex materials to assist the signal output, which increases the cost of detection.[14]

Inductively coupled plasma mass spectrometry (ICP-MS) in conjunction with the element labeling technique represents an advancement in pathogen detection. This combination effectively overcomes the limitations of optical and electrochemical biosensors, such as spectral overlap, background scattering, and interference from the biological matrix. ICP-MS is capable of precise chemical characterization and quantification of trace and ultratrace elements in biological materials,[24] establishing itself as a superior tool for multivariate and accurate biological analysis with remarkable sensitivity and wide detection range. Recent studies have demonstrated the combination of specially designed metal nanoparticles with ICP-MS for pathogen detection.[25–28] Protein probe-modified nanoparticles can target the specific surface proteins on pathogens *via* immunological antibody–antigen recognition,[29,30] facilitating accurate pathogen detection. However, this method relies on the availability of highly specific antibodies or probes for accurate pathogen identification, with diagnostic precision depending on the affinity and specificity of these antibodies or probes. Cross-reactivity with similar pathogens may result in false positive or negative signals.[31] In contrast, nucleic acid probe-modified nanoparticles may offer improved specificity.[32,33] Nonetheless, designing highly specific nucleic acid probes and developing the nanocarriers with optimal specific surface area presents significant challenges.

In this study, we introduced a highly sensitive *S. typhimurium* detection method that utilizes a novel combination of popcorn-sharped AuNPs and magnetic nanoparticles (MNPs) with a cluster structure to target *S. typhimurium* DNA *via* sandwich hybridization (Fig. 1). We designed capture and report probes to bind conserved sequences of *S. typhimurium* DNA, allowing specific recognition. The large surface area of the popcorn-shaped AuNPs, functionalized with reporter probes, provides efficient capture of target *S. typhimurium* DNA. Each popcorn-shaped AuNP contains hundreds of millions of Au atoms. These atoms contribute to the generation of robust signals in ICP-MS, thereby significantly enhancing the sensitivity. Simultaneously, cluster-structured MNPs, functionalized with capture probes, enable magnetic separation of the formed MNPs-*S. typhimurium* DNA-AuNPs sandwich-structure complexes. Quantitative detection of *S. typhimurium* is achieved by analyzing the Au content within these complexes using ICP-MS. This approach offers rapid detection, high sensitivity, wide detection range, and enhanced specificity. It advances the *S. typhimurium* detection strategy and provides a versatile framework for the development of prompt and accurate pathogen detection technologies, crucial for managing emergent pathogen infection events.

2. Experimental

2.1. Chemicals and materials

Anhydrous ferric chloride (FeCl₃), ethylene glycol (EG), diethylene glycol (DEG), sodium acetate (NaOAc), polyvinylpyrrolidone (PVP, K-30), 3-glycidoxypropyltrimethoxylsilane (GPTMS), chloroauric acid tetrahydrate (HAuCl·4H₂O), ascorbic acid (AA), hydroxylammonium chloride (NH₂OH·HCl), potassium carbonate anhydrous (K₂CO₃) and dithiothreitol (DTT) were purchased from Sigma-Aldrich Chemical Co.

2.2. Design of capture probe and report probe for the detection of *S. typhimurium* DNA

The genome-wide information of *S. typhimurium* was searched in the National Center for Biotechnology Information (NCBI) database, and the genome file was downloaded (GenBank assembly accession: GCA_016864495.1), which yielded a total of 4 870 244 bp of genome-wide information. The whole genome information was imported into Geneious for the invA gene sequence. The invA gene sequences (5′-TCCTCAACTTCAGCAGATACCATTACTGCTCGTA-ATTCGCCGCCATTGGCGAATTTATGACAAATATAACGCGCCATTGC-TCCACGAATATGCTCCACAAGGT-3′) was selected as the target gene for the detection of this experiment.

The obtained invA gene sequences were imported into Primer Premier 6.0 to design the capture probe and report probe. The thiolated capture probe (5′-HS-(CH₂)₆-(A)₁₂-ACCT-TGTGGAGCATATTCG-3′) and report probe (5′-GTATCTGCTGA-AGTTGAGGA-(A)₁₂-(CH₂)₆-SH-3′) were designed to be complementary to the target. All oligonucleotide sequences were synthesized and purified by high-performance liquid chromatography (HPLC). All oligonucleotides were dissolved in Tris-EDTA (TE) buffer (10 mM Tris-HCl, 1 mM EDTA, pH 8) and kept at −20 °C.

2.3. Preparation of capture probe-grafted MNPs

MNPs were synthesized following a previously reported method.[34] Briefly, 2 mmol FeCl₃ was added into a mixture of 4 mL EG and 16 mL DEG in a 50 mL two-necked flask followed by continuous stirring for 30 min at room temperature (RT). After adding 2 g PVP (K-30), the two-necked flask was placed in a 125 °C oil bath, and the mixture was stirred for 1 h. Subsequently, 1.5 g NaOAc was added into the flask and stirred for 30 min at RT. The mixture in the two-necked flask was poured into a 50 mL

Jieyu Zhang is currently an Associate Professor in the National Engineering Research Center for Biomaterials and the College of Biomedical Engineering, Sichuan University. She holds a Master of Engineering degree in Polymer Materials from Beijing University of Chemical Technology, China, and earned her PhD from National University of Singapore in 2016. Dr Zhang's research is focused on the innovation and application of electroactive biomaterials, exploring their potential in enhancing biomedical devices, healthcare products, and in vitro diagnostic tools. Her work continues to push the boundaries of biomaterial science, contributing to advancements in biomedical and healthcare technology.

Jieyu Zhang

7312 | *J. Mater. Chem. B*, 2024, **12**, 7311–7323

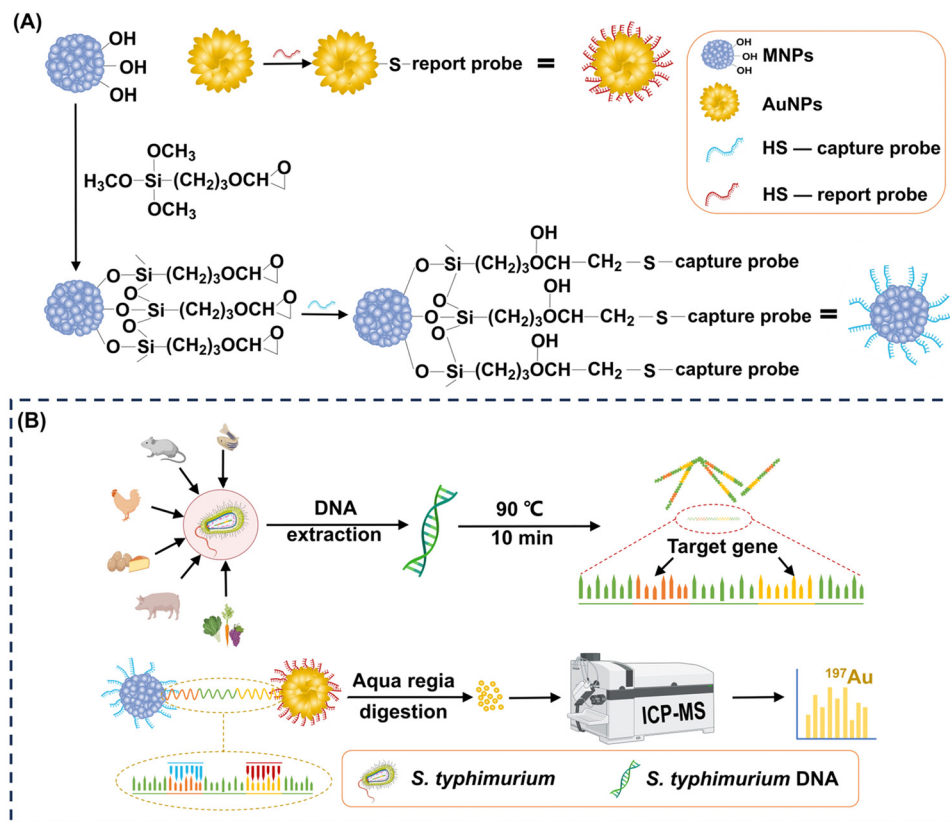This journal is © The Royal Society of Chemistry 2024

Fig. 1 Schematic illustration of (A) preparation of report probe-grafted AuNPs and capture probe-grafted MNPs and (B) *S. typhimurium* detection by sandwich hybridization using the report probe-grafted AuNPs and capture probe-grafted MNPs with ICP-MS analysis.

stainless-steel autoclave lined with Teflon, and this autoclave was subjected to heating in an oven at 200 °C for 12 h. The autoclave content was centrifuged at 10 621 g for 15 min to separate the supernatant from the MNPs. The collected MNPs were washed three times with ethanol and Milli-Q water, followed by drying in a vacuum oven for 12 h.

The obtained MNPs were functionalized with epoxy groups utilizing a silanization agent. Specifically, 0.5 mL of GPTMS was added into 50 mL of a 0.4% (w/v) MNP suspension in toluene. The mixture was sonicated for 30 min to ensure homogeneity and then refluxed for 12 h under a N_2 atmosphere. The epoxy-functionalized MNPs were isolated from the solution by magnetic attraction and purified by sequential washing with toluene, ethanol, and Milli-Q water. The epoxy-functionalized MNPs were finally obtained after 12 h of vacuum drying.

Before coupling the thiolated capture probes to the epoxy-functionalized MNPs, a reductive cleavage step was performed to cleave the disulfide bonds. In brief, 50 μL of a 2 nM thiolated capture probe solution was treated with 100 μL of a 0.1 M DTT solution in TE buffer for 3 h. The resulting probe solution was purified using a NAP-5 column (Cytiva, USA) to remove excess DTT and salt matrix following the manufacturer's protocol. The concentration of the purified probe solution was measured using a Nanodrop spectrophotometer (Thermo, USA).

To graft the thiolated capture probes onto the epoxy-functionalized MNPs, 0.39 mg of the epoxy-functionalized MNPs were initially dispersed in 200 μL of a 50 mM Tris-HCl buffer (pH 8). Then, 480 μL of the capture probe solution at different concentrations was introduced into the suspension, and the mixture was incubated at RT for different durations. The resulting capture probe-grafted MNPs were isolated by magnetic separation, washed three times with TE buffer, and re-suspended in 200 μL of TE buffer. The grafting parameters, including capture probe concentration (0.23, 0.45, 0.66, 0.90, and 1.13 ng μL^{-1}), and reaction duration (0.17, 0.5, 1, 2, 4, 6, 8, and 24 h) were optimized to achieve the maximum grafting density. The optimal grafting density of the capture probes on the epoxy-functionalized MNPs was achieved with a capture probe concentration of 0.66 ng μL^{-1} and an incubation time of 8 h. Detailed calculations regarding the grafting density of the capture probes on the epoxy-functionalized MNPs are provided in the ESI.†

2.4. Preparation of report probe-grafted AuNPs

Popcorn-shaped AuNPs were synthesized using a template-free method.[35] Initially, 1 mL of a 0.2 M K_2CO_3 solution was mixed with 25 mL of a 2.4×10^{-4} M $HAuCl_4$ solution. Subsequently, 5 μL of a 10 mM AA solution was introduced to reduce Au^{3+} to generate Au seeds. After 5 min of reaction, different volumes of a 10 mM NH_2OH solution (0, 500, 1000, and 2000 μL) were rapidly injected to induce the formation of popcorn-shaped AuNPs. This transformation was indicated by an immediate

This journal is © The Royal Society of Chemistry 2024

J. Mater. Chem. B, 2024, **12**, 7311–7323 | **7313**

change in the color of the suspension from light yellow to dark blue. The popcorn-shaped AuNPs were harvested by centrifugation at 956 g for 6 min, followed by washing twice with Milli-Q water and drying in a vacuum oven for 12 h.

The thiolated report probes were pretreated by DTT to cleave disulfide bonds before grafting onto the AuNPs. For grafting, 0.74 mg AuNPs were ultrasonically dispersed in 200 μL of TE buffer. Subsequently, 480 μL of the capture probe solution at different concentrations was introduced into the AuNPs suspension. The mixtures were incubated at RT for different durations. The resulting report probe-grafted AuNPs were isolated by centrifugation, washed three times with TE buffer, and re-suspended in 200 μL of TE buffer. The grafting parameters, including the report probe concentration (0.23, 0.46, 0.69, 0.93, and 1.16 ng μL^{-1}), and reaction duration (0.17, 0.5, 1, 2, 4, 6, 8, and 24 h) was optimized to maximize grafting density. The optimal condition was identified when 0.93 ng μL^{-1} of report probes were used with a reaction duration of 8 h. The calculation of the grafting density of the report probes on the AuNPs is detailed in the ESI.†

2.5. Nanoparticle characterization

The morphology and zeta potential of the synthesized nanoparticles were analyzed by transmission electron microscopy (TEM; Zeiss, Germany) and Zetasizer Nano (Malvern, UK), respectively. The crystal structures of the MNPs and epoxy-functionalized MNPs were analyzed by X-ray diffraction (XRD; Bruker, Germany) at a voltage of 40 kV, a current of 300 mA, and a scanning rate of 2° min^{-1} with step size 0.01°. The magnetic properties of the MNPs and epoxy-functionalized MNPs were measured using vibrating sample magnetometry (VSM; Lake Shore, USA). The chemical structure of the MNPs and epoxy-functionalized MNPs was characterized using attenuated total reflectance Fourier transform infrared spectroscopy (ATR-FTIR Spectrometer; Thermo, USA) and X-ray photoelectron spectroscopy (XPS; Kratos, UK).

2.6. *S. typhimurium* DNA extraction

S. typhimurium bacteria were cultured in lysogeny broth for 48 h, and harvested by centrifugation at 15 294 g for 1 min. *S. typhimurium* DNA was extracted according to the protocol of the TIANamp Bacteria DNA Kit (TIANGEN, Beijing), and stored at −20 °C for further use.

2.7. Capture of *S. typhimurium* DNA by capture probe-grafted MNPs

The stock solution of *S. typhimurium* DNA was heated at 90 °C for 10 min to unwind the double helix. Then, 10 μL of the resultant DNA solution at a concentration of 10^{11} copies mL^{-1} was incubated with 45 μL of the capture probe-grafted MNP suspension at different concentrations (10^{-3}, 10^{-2}, 10^{-1}, 1, and 10 ng μL^{-1}). The hybridization was conducted over various durations (10, 20, 30, 40, 50, and 60 min) at 37 °C under continuous shaking at 200 rpm. After hybridization, the *S. typhimurium* DNA-MNP complexes were harvested by magnetic separation. The concentration of unbound *S. typhimurium* DNA in the supernatant was quantified with the Nanodrop spectrophotometer, enabling the determination of the capture efficiency of the capture probe-grafted MNPs for *S. typhimurium* DNA. The methodology for this calculation is elaborated in the ESI.† Optimal capture efficiency, 78.3%, was achieved with the capture probe-grafted MNP suspension at 1 ng μL^{-1} and a hybridization period of 40 min.

2.8. Capture of *S. typhimurium* DNA by report probe-grafted AuNPs

The hybridization protocol for the report probe-grafted AuNPs with *S. typhimurium* DNA paralleled that of the capture probe-grafted MNPs, with the exception the report probe-grafted AuNPs concentration due to their different probe grafting density. To optimize the capture efficiency, the report probe-grafted AuNP suspension at different concentrations (2.5 × 10^{-3}, 2.5 × 10^{-2}, 2.5 × 10^{-1}, 2.5, and 25 ng μL^{-1}) were explored. After hybridization, the *S. typhimurium* DNA-AuNP complexes were isolated by centrifugation at 956 g for 5 min. Optimal capture efficiency, 72.8%, was obtained with the report probe-grafted AuNP suspension at 2.5 ng μL^{-1} over a hybridization period of 50 min. The methodology for efficiency calculation is detailed in the ESI.†

2.9. Formation of sandwich-structure complexes of MNPs-*S. typhimurium* DNA-AuNPs

For the formation of the sandwich-structure complexes, 45 μL of the capture probe-grafted MNP suspension at 1 ng μL^{-1} and 45 μL of the report probe-grafted AuNP suspension at 2.5 ng μL^{-1} were incubated with 10 μL of a *S. typhimurium* DNA solution for 50 min at 37 °C under shaking at 200 rpm. The concentration of *S. typhimurium* DNA in the hybridization assay ranged from 10^1 to 10^{10} copies mL^{-1}. The resultant composites were collected by magnetic separation and washed with 5 mL of TE buffer.

2.10. ICP-MS analysis

The sandwich-structure complexes were digested with aqua regia, after which the sample volume was adjusted to 10 mL. The sample solution containing the dissolved Au ions were introduced into the Agilent 7800 ICP-MS (Agilent Technologies, Japan) to detect Au at m/z 197. The specific models and operating parameters used for Au determination are detailed in Table S1 in the ESI.†

2.11. Anti-interference assay

To evaluate the specificity of our method for *S. typhimurium* DNA detection, 45 μL of the capture probe-grafted MNPs at 1 ng μL^{-1} and 45 μL of the report probe-grafted AuNP suspension at 2.5 ng μL^{-1} were incubated with 10 μL of DNA from ten different pathogens *Haemophilus influenzae* (*H. influenzae*), *Streptococcus pneumoniae* (*S. pneumoniae*), *Escherichia coli* (*E. coli*), β-hemolytic streptococcus (BHS), CTB, α-hemolytic streptococcus (AHS), *Neisseria meningitidis* (*N. meningitidis*), *Streptococcus pyogenes* (*S. pyogenes*), *Lactobacillus acidophilus* (*L. acidophilus*), and *Pseudomonas aeruginosa* (*P. aeruginosa*), each at a concentration of 10^5 copies mL^{-1}, for 50 min at 37 °C under shaking at 200 rpm. After that, the composites were

7314 | *J. Mater. Chem. B*, 2024, **12**, 7311–7323

This journal is © The Royal Society of Chemistry 2024

harvested from the mixture *via* magnetic separation and washed with 5 mL of TE. We also tested the performance of our method in detecting a low concentration of target *S. typhimurium* from high concentrations of interference bacterial DNA (*H. influenzae*, *S. pneumoniae*, *E. coli*, BHS, and CTB). In detail, we measured 10^2 copies mL^{-1} of *S. typhimurium* DNA in the presence of 10^9 copies mL^{-1} of DNA from each of the five aforementioned interference bacteria. In addition, signals from a mixed sample containing both high concentrations of all the five interference bacterial DNAs and the low concentration of *S. typhimurium* DNA were analyzed. Detailed information on the five interference bacteria is provided in ESI† Table S2.

2.12.   Repeatability assay

To evaluate the repeatability of our method for *S. typhimurium* DNA detection, five samples containing the same concentration (10^5 copies mL^{-1}) of *S. typhimurium* DNA were assessed. Specifically, 45 µL of the capture probe-grafted MNPs (1 ng $µL^{-1}$) and 45 µL of the report probe-grafted AuNPs (2.5 ng $µL^{-1}$) were incubated with 10 µL of *S. typhimurium* DNA (10^5 copies mL^{-1}) for 50 min at 37 °C under shaking at 200 rpm. After that, the sandwich-structure complexes were harvested from the mixture *via* magnetic separation and washed with 5 mL of TE buffer. After 5 cycles of washing, the Au concentration in the complexes was measured by ICP-MS.

2.13.   Performance in biological samples

To further investigate the practical application, the detection assay was conducted in biological samples. The *S. typhimurium*

DNA was dissolved in fetal bovine serum (FBS; Gibco, New Zealand), urine, simulated body fluid (SBF; LEAGENE Biotechnology, China), or drink (Mizone®, Danone, China). The detection assay was performed following the procedure described in Section 2.12.

2.14.   Statistical analysis

One-way analysis of variance (ANOVA) and two-way ANOVA were used to analyze the differences among groups. Significance levels were defined as $*P < 0.05$, $**P < 0.01$, $***P < 0.001$, $****P < 0.001$. All statistical analyses were performed using Graph Pad. Prism 10.1.

3.   Results and discussion

3.1.   Characterization of capture probe-grafted MNPs

3.1.1.   MNPs. MNPs were synthesized through a hydrothermal process comprising a sequence of intricate chemical reactions. The lone electron pairs on the N and O atoms within the polar moiety of the surfactant PVP occupied the electronic orbits of Fe^{3+}, resulting in the formation of $Fe(OH)_3$ precursors. Under the high-temperature and high-pressure conditions within the hydrothermal reactor, $Fe(OH)_3$ precursors were dehydrated to yield Fe_3O_4 seeds. The presence of PVP on the surface of these seeds restricted their growth. Driven by high surface binding energy and magnetic dipole moment forces, the Fe_3O_4 seeds aggregated to form more stable Fe_3O_4 MNPs.
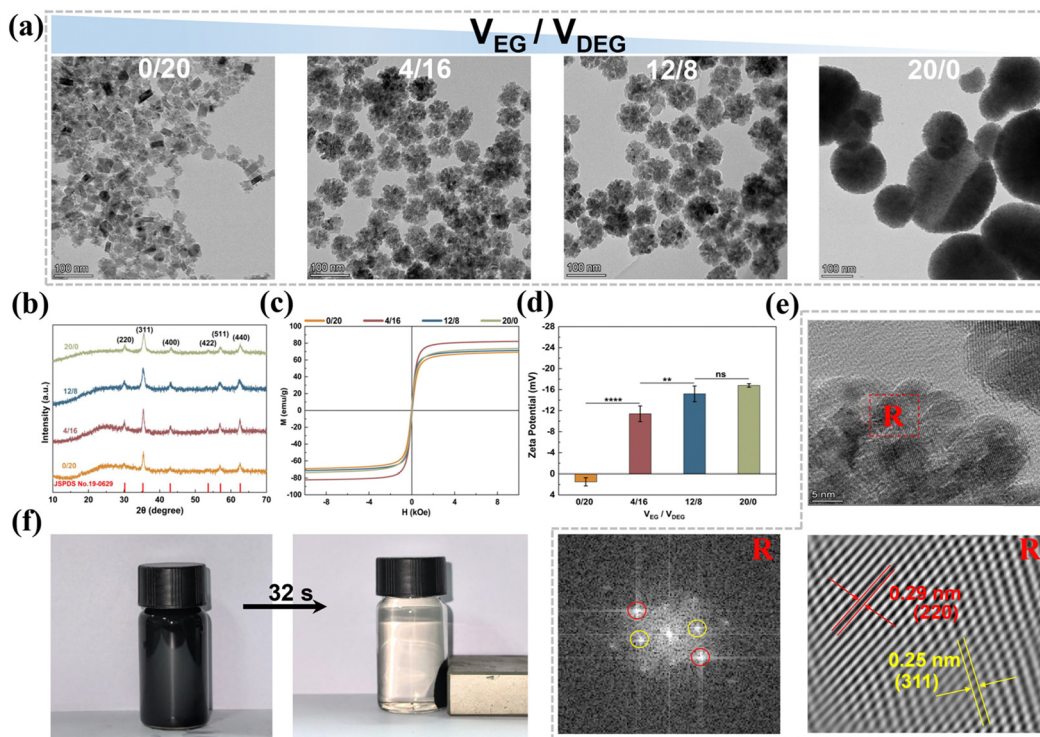

Fig. 2   Characterization of MNPs synthesized with different V_{EG}/V_{DEG} ratios. (a)–(d) TEM images (a), XRD spectra (b), $M–H$ curves (c), and zeta potential (d) of MNPs synthesized with V_{EG}/V_{DEG} ratios of 0/20, 4/16, 12/8, and 20/0. (e) HRTEM images of MNPs synthesized with V_{EG}/V_{DEG} ratio of 4/16. (f) Digital photos of MNPs dispersed in water (left) and collected by magnetic separation (right).

The MNPs appeared as clusters with a rough and irregular surface (Fig. 2a), which greatly expanded the specific surface area relative to spherical MNPs of identical diameter, offering more binding sites for subsequent surface functionalization. The size of the synthesized MNPs can be controlled by adjusting the volume ratio of the binary solvent system, comprising EG and DEG. The average diameter of MNPs increased progressively from 12 ± 2 nm to 188 ± 75 nm, when the volume ratio of EG/DEG (V_{EG}/V_{DEG}) was tuned from 0/20 to 20/0 (Fig. 2a). This size modulation is directly correlated with the viscosity of the binary solvent system. Lower solvent viscosity facilitated more rapid aggregation of the Fe_3O_4 seeds, resulting in larger MNPs.[36]

Fig. 2b shows the XRD patterns of the MNPs prepared with different V_{EG}/V_{DEG} ratios. These patterns were consistent with the cubic-phase Fe_3O_4 spectrum (PDF#88-0866). The diffraction peaks at $30.1°$, $35.4°$, $43.1°$, $53.4°$, $57°$, and $62.6°$ corresponded to the (220), (311), (400), (422), (511), and (440) crystal planes of magnetite, respectively.[37] The average crystallite size of Fe_3O_4 MNPs prepared at $V_{EG}/V_{DEG} = 0/20$ was calculated to be 18.9 nm using the Debye–Scherrer equation ($D_{hkl} = k\lambda/\beta \cos\theta$),[36] with the full width at half maximum of the primary (311) diffraction peak. Furthermore, the diffraction peaks of the MNPs broadened with increasing V_{EG}/V_{DEG} ratio, implying the aggregation of the Fe_3O_4 seeds.[36] The crystallite sizes estimated from XRD are in agreement with the dimensional changes observed by TEM (Fig. 2a).

The magnetic absorption performance of the MNPs was evaluated by RT hysteresis loop measurements using a vibrating sample magnetometer (Fig. 2c). All the MNPs, synthesized with different V_{EG}/V_{DEG} ratios, exhibited hysteresis loops without coercivity or remanence, indicating their superparamagnetic characteristics.[38] The magnetic saturation (M_s) values of the MNPs synthesized with V_{EG}/V_{DEG} ratios of 0/20, 4/16, 12/8, and 20/0, were recorded as 69.2, 82.0, 71.3, and 73.7 emu g^{-1}, respectively. The MNPs obtained with a V_{EG}/V_{DEG} ratio of 4/16 achieved the highest M_s value, indicating a superior magnetic response suitable for enhanced magnetic separation applications.

In addition to magnetic separation capability, the colloidal stability of the MNPs in aqueous solution is important for their biomedical application. To evaluate this, the zeta potential of the MNPs was assessed. As shown in Fig. 2d, the MNPs produced with a V_{EG}/V_{DEG} ratio of 0/20 exhibited a positive zeta potential of 1.49 mV, which is indicative of a greater tendency for aggregation. Conversely, increasing the V_{EG}/V_{DEG} ratio from 4/16 to 20/0 resulted in a negative shift in zeta potential from -11.4 mV to -16.8 mV, implying improved colloidal stability.[39]

The MNPs obtained with a V_{EG}/V_{DEG} ratio of 4/16 were selected for subsequent investigation, due to their optimal magnetic response, high specific surface area, and enhanced colloidal stability. Morphological examination of the MNPs prepared from three independent batches at this V_{EG}/V_{DEG} ratio revealed uniformly clustered structures with a particle size of 64 ± 12 nm (Fig. S10, ESI†), indicating reproducible synthesis with consistent structural and dimensional characteristics across batches. High-resolution TEM (HRTEM) further confirmed their crystallinity, with interplanar spacings of 0.25 and 0.29 nm aligning with the (311) and (220) lattice planes

of cubic Fe_3O_4 magnetite, respectively (Fig. 2e).[37] Additionally, these MNPs displayed a rapid and efficient magnetic response, achieving complete alignment in 32 s upon application of an external magnetic field (Fig. 2f).

3.1.2. Epoxy-functionalized MNPs. The MNPs were functionalized with epoxy groups through a reaction with GPTMS as confirmed by ATR-FTIR spectra (Fig. 3a). The ATR-FTIR spectrum of the MNPs showed a strong band at 550 cm^{-1}, which is attributed to the Fe–O stretching vibrations.[40] For the epoxy-functionalized MNPs, the spectrum showed characteristic bands belonging to Si–O groups of GPTMS at 928 and 1071 cm^{-1}, and the bands related to the propyl groups of GPTMS at 2850 and 2927 cm^{-1} (Fig. S1, ESI†), indicating the presence of the silane layer on the MNPs.[41] The epoxy functionalization was further evidenced by the C–O–C vibration at 1274 cm^{-1}, along with Si–C and –CH$_2$ vibrations at 1208 and 1421 cm^{-1}, respectively.[42]

The chemical state and surface groups of the epoxy-functionalized MNPs were further verified by XPS analysis (Fig. 3b–f). The wide scan XPS spectra revealed the presence of Fe, O, and C elements in the MNPs, with an additional Si signal detected in the epoxy-functionalized MNPs (Fig. 3b). High-resolution XPS spectra deconvolution of C 1s (Fig. 3c) and O 1s (Fig. 3d) provided insight into the molecular structure changes following GPTMS silanization of the MNPs. The asymmetric and broad C 1s spectrum of the MNPs was deconvoluted into four peaks at binding energies of 284.5, 285.6, 286.1, and 288.4 eV, which can be attributed to the C–C, C–N, C–O–C, and C = O bonds, respectively (Fig. 3c).[43] The presence of these peaks confirms the incorporation of PVP as a stabilizer during MNP synthesis. After epoxy-functionalization, the high-resolution C 1s XPS spectrum showed four deconvoluted peaks at 284.8, 283.2, 285.9, and 288.2 eV (Fig. 3c).[43] These peaks correspond to the C–C bonds in the alkane chain of the silane layer, Si–C bonds indicative of silane coupling, the C–O–C ether linkages of the epoxy groups, and C=O bonds in the silane layer, respectively.[42] For the O 1s high-resolution spectrum, the MNPs displayed three sub-peaks at 529.2, 530.6, and 533.1 eV, which are attributed to the Fe–O, O–C/O=C and O–C=O bonds, respectively. GPTMS silanization led to a Fe–O–Si peak at 531.6 eV and shifted the binding energy of the O–C/O=C and O–C=O bonds by approximately 1.1 eV (Fig. 3d),[44] suggesting that silanization induced the conductivity reduction and electron cloud density changes of the MNPs.[45] Furthermore, the Si 2p peak at 101.6 eV was detected in the spectrum of the epoxy-functionalized MNPs (Fig. 3e), which is attributed to the Si–O bonds in the silane layer.[46] For the Fe 2p high-resolution spectra (Fig. 3f), the fitting peaks at 722.1 and 709.3 eV were consistent with the Fe–O bonds of ferrite, suggesting that the epoxy-functionalization did not alter the MNP core.[43] XRD analysis further supports this preservation, the diffraction peaks at 2θ values of $30.1°$, $35.4°$, $43.1°$, $53.4°$, $57.0°$, and $62.6°$ remained consistent for the MNPs after epoxy-functionalization (Fig. 3g). These peaks corresponded to the crystalline planes (220), (311), (400), (422), (511) and (440) of the Fe_3O_4 crystal, indicating core structure integrity.[37]

The epoxy-functionalization resulted in a more negative zeta potential (-28.1 mV) for the MNPs (Fig. S2, ESI†). This

7316 | *J. Mater. Chem. B*, 2024, **12**, 7311–7323

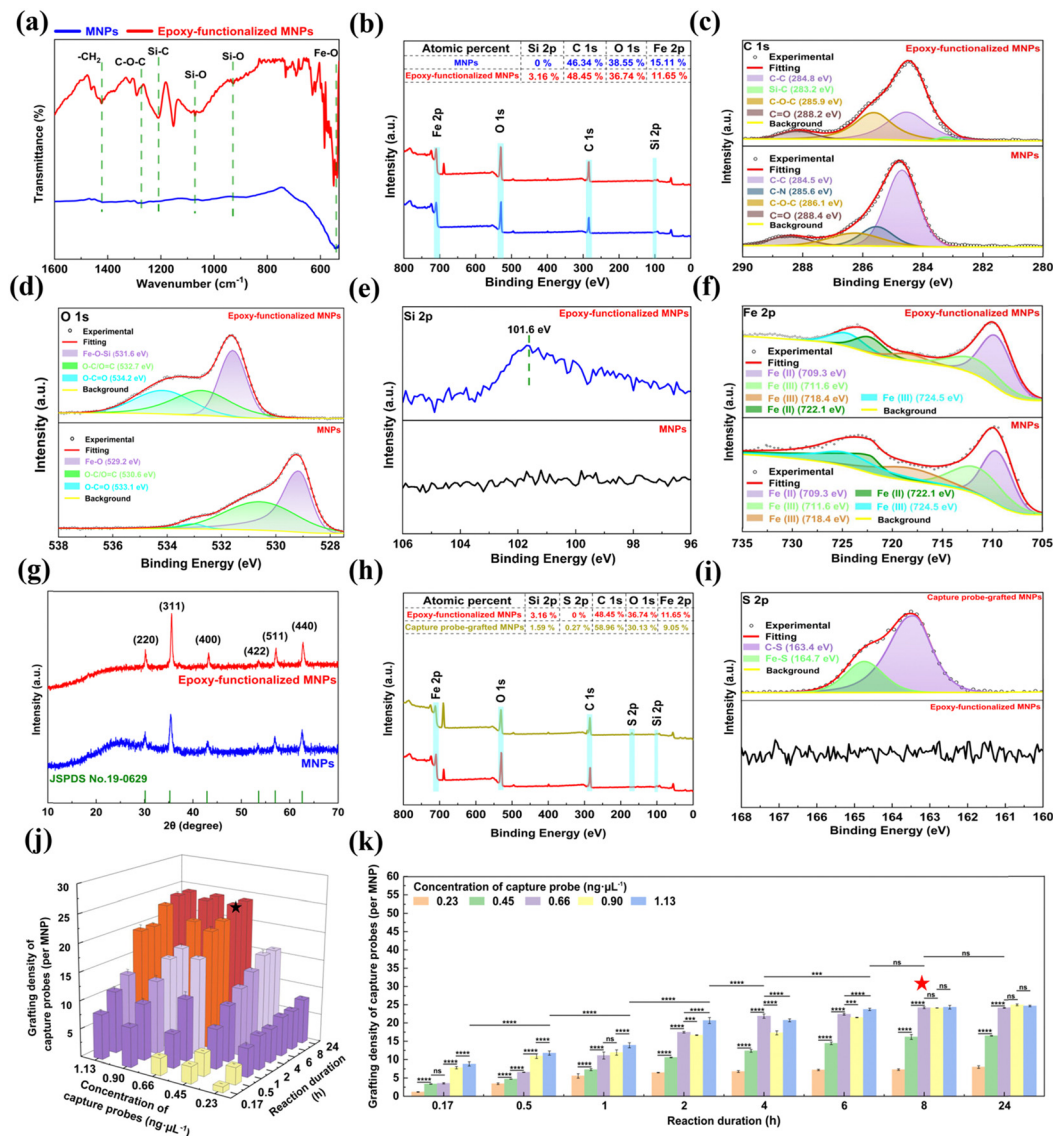This journal is © The Royal Society of Chemistry 2024

Fig. 3 Characterization of epoxy-functionalized MNPs and capture probe-grafted MNPs. (a) and (b) ATR-FTIR (a) and wide-scan XPS (b) spectra comparing MNPs and epoxy-functionalized MNPs. (c)–(f) High-resolution C 1s (c), O 1s (d), Si 2p (e), and Fe 2p (f) XPS spectra comparing MNPs and epoxy-functionalized MNPs. (g) XRD spectra comparing MNPs and epoxy-functionalized MNPs. (h) and (i) Wide-scan (h) and high-resolution S 2p (i) XPS spectra comparing epoxy-functionalized MNPs and capture probe-grafted MNPs. (j) and (k) Capture probe grafting density on epoxy-functionalized MNPs as a function of capture probe concentration and reaction duration (j), and the corresponding statistical analysis of the grafting density (k).

alternation enhanced the colloidal stability and dispersibility of the epoxy-functionalized MNPs, beneficial to subsequent conjugation with thiolated capture probes for the detection of *S. typhimurium* DNA.[39] Besides, the magnetic properties of the MNPs were retained after the epoxy-functionalization, as evidenced by the similar RT hysteresis loops before and after GPTMS modification, and the high M_s value of the epoxy-functionalized MNPs (73.4 emu g^{-1}) (Fig. S3, ESI†). This feature is critical to ensure rapid and efficient magnetic separation during the detection of *S. typhimurium*.

3.1.3. Capture probe-grafted MNPs. To establish a stable, covalent linkage between the MNPs and capture probes for robust detection of *S. typhimurium*, thiol–epoxy "click" chemistry was employed. This choice was guided by the mild and

controlled reaction conditions, coupled with the high efficiency and specificity of the thiol–epoxy interaction.[47] In mildly alkaline Tris-HCl buffer (pH 8), the thiol groups on the thiolated capture probes acted as nucleophiles, initiating the opening of the epoxy groups on the epoxy-functionalized MNPs. This process resulted in the formation of thioether bonds, ensuring the stable integration of the capture probes on the MNPs. The capture probe conjugation was evidenced by a 10 nm redshift of the absorption peak from 245 nm to 255 nm in the UV-vis spectra (Fig. S4, ESI†).[48] The surface chemical state of the capture probe-grafted MNPs was further verified by XPS analysis (Fig. 3h–i). The wide-scan XPS spectrum of the capture probe-grafted MNPs revealed an additional S 2p peak (Fig. 3h), which can be deconvoluted into two peaks at 163.4 and 164.7 eV, corresponding to the C–S

This journal is © The Royal Society of Chemistry 2024

J. Mater. Chem. B, 2024, **12**, 7311–7323 | **7317**

and Fe–O bonds, respectively (Fig. 3i).[49] These findings confirm the successful immobilization of the capture probes onto the epoxy-functionalized MNPs.

To optimize the conjugation process of the capture probes onto the epoxy-functionalized MNPs, the effect of the capture probe concentration and reaction duration on the grafting density of the capture probes on the epoxy-functionalized MNPs was systematically investigated (Fig. 3j and k). For reaction duration less than 8 h, the grafting density on the MNPs increased with the capture probe concentration up to 1.13 ng μL^{-1}. When the reaction duration ≥ 8 h, the grafting density also increased but reached a plateau at a capture probe concentration of 0.66 ng μL^{-1}. At a fixed capture probe concentration of 0.66 ng μL^{-1}, the grafting density augmented as the reaction duration extended, plateauing at 8 h. This plateau indicates a saturation of the available epoxy sites on the MNPs. Therefore, the optimal conjugation conditions were determined to be a capture probe concentration of 0.66 ng μL^{-1} and a reaction time of 8 h, which corresponded to an average of approximately 24 capture probes grafted onto each MNP. Further details on the grafting density calculations of the capture probes on the epoxy-functionalized MNPs were provided in the ESI.†

3.2. Characterization of report probe-grafted AuNPs

3.2.1. Characterization of AuNPs. Au was selected as the analytical marker for the ICP-MS analysis in *S. typhimurium*

detection, due to its low abundance and chemical inertness within biological matrices.[50] These characteristics help to minimize background noise and eliminate interference from coexisting species, thereby significantly improving the specificity and accuracy of detection. Moreover, AuNPs comprising thousands of Au atom clusters serve to amplify *S. typhimurium* signals, thus enhancing detection sensitivity.

Herein, we synthesized AuNPs *via* a facile and efficient method, which involves a two-step reduction process. Initially, $AuCl_4^-$ ions are reduced by AA to generate small Au seeds. Subsequently, these Au seeds serve as nucleation sites for further reduction and deposition of Au atoms by NH_2OH, ultimately yielding popcorn-shaped AuNPs.[35] Notably, this protocol is surfactant-free and operates at RT, with a rapid reaction time of 18 min. The size of the resultant AuNPs can be easily adjusted by varying the volume of the 10 mM NH_2OH solution added (Fig. 4a). In the absence of NH_2OH, only the initial Au seeds with a diameter of 10 ± 2 nm were observed. The introduction of NH_2OH triggers a reduction of Au atoms and their subsequent deposition onto the seeds, promoting their aggregation into the unique popcorn-like structures. Increasing the volume of the NH_2OH solution from 500 μL to 2000 μL led to the growth of the AuNPs from 60 ± 7 nm to 94 ± 14 nm in diameter. The specific surface area of the prepared popcorn-shaped AuNPs was quantified using Brunauer–Emmett–Teller (BET) analysis (Fig. S5, ESI†). The popcorn-shaped AuNPs had a
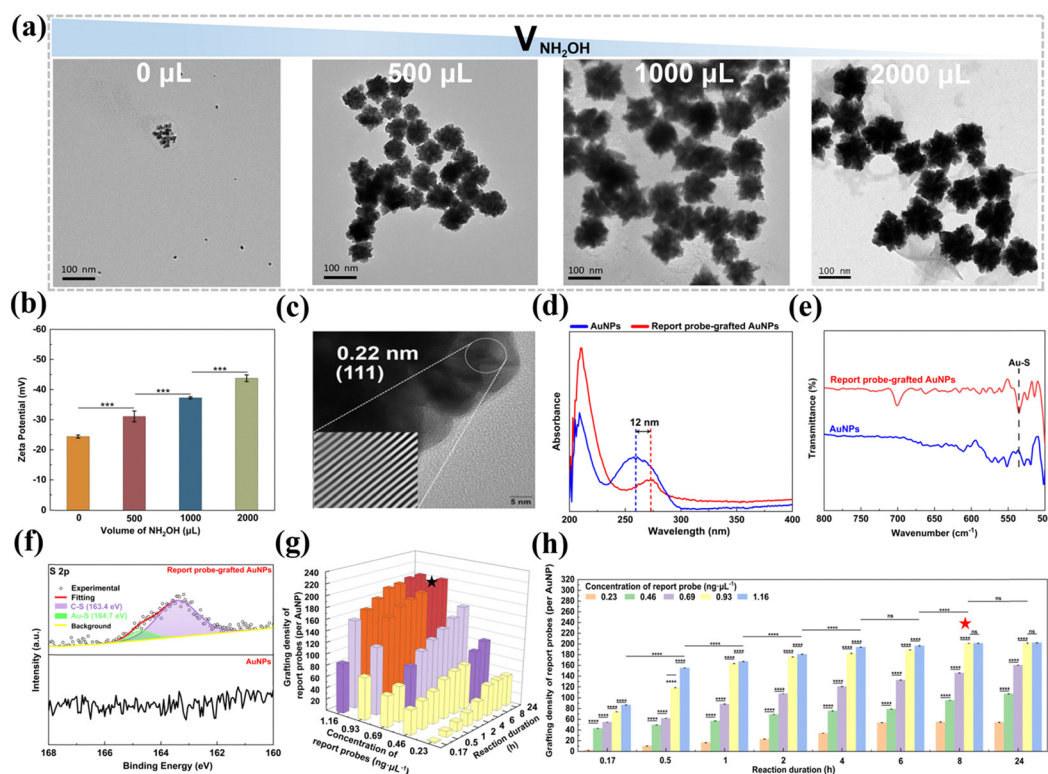

Fig. 4 Characterization of AuNPs and report probe-grafted AuNPs. (a) and (b) TEM images (a) and zeta potential (b) of AuNPs synthesized with different NH_2OH volumes (0, 500, 1000, and 2000 μL). (c) HRTEM images of AuNPs synthesized with 1000 μL of a 10 mM NH_2OH solution. (d)–(f) UV-vis spectra (d), ATR–FTIR spectra (e), and high-resolution S 2p XPS spectra (f) comparing AuNPs and report probe-grafted AuNPs. (g) and (h) Report probe grafting density on AuNPs as a function of report probe concentration and reaction duration (g), and the corresponding statistical analysis of the grafting density (h).

7318 | *J. Mater. Chem. B*, 2024, **12**, 7311–7323

This journal is © The Royal Society of Chemistry 2024

larger specific surface area (10.64 m^2 g^{-1}), compared to their spherical counterparts (3.53 m^2 g^{-1}) with the same diameter (88 nm). This enhanced surface area provided additional binding sites for the thiolated reporter probes, allowing the grafting of a larger number of reporter probes to the AuNPs. This configuration broadened the detection range and lowered the detection limit for *S. typhimurium* DNA.

The zeta potential of AuNPs synthesized with different volumes of a 10 mM NH$_2$OH solution was analyzed to assess their colloidal stability. Fig. 4b shows that the AuNPs were negatively charged, and their zeta potential became more negative as the NH$_2$OH volume increased. This trend suggests that the colloidal stability was enhanced with higher NH$_2$OH volumes, attributed to stronger electrostatic repulsion between the AuNPs that reduced the likelihood of aggregation, and thus improved the stability of the AuNP dispersion.[39] Specifically, the AuNPs generated with 1000 μL of the 10 mM NH$_2$OH solution exhibited a zeta potential of −37.3 ± 0.35 mV, less negative than the zeta potential of −43.8 ± 1.10 mV observed for the AuNPs synthesized with 2000 μL. Despite the reduced zeta potential, the AuNPs produced with 1000 μL of the 10 mM NH$_2$OH solution displayed a smaller diameter (88 ± 12 nm) than those prepared with 2000 μL (94 ± 14 nm). Given the importance of maximizing specific surface area alongside maintaining colloidal stability for the efficient and sensitive detection of *S. typhimurium*, the AuNPs synthesized with 1000 μL of the 10 mM NH$_2$OH solution were selected for further exploration due to their smaller size characteristics and acceptable stability. HRTEM analysis further confirmed the crystalline nature of the AuNPs, with interplanar spacings of 0.22 nm aligning with the (111) lattice planes of face-centered cubic Au (Fig. 4c).[51]

3.2.2. Report probe-grafted AuNPs. The report probes conjugated with the AuNPs *via* the reaction between the thiol groups on the thiolated report probes and the AuNP surface, leading to the formation of stable Au–S covalent bonds (Fig. 1).[52] The conjugation process was monitored using UV-vis spectroscopy (Fig. 4d), where a 12 nm redshift in the absorption peak from 258 nm indicated the successful immobilization of the report probes onto the AuNP surface.[53] The covalent bonding between the report probes and the AuNPs was further verified by ATR-FTIR and XPS. The ATR-FTIR spectrum (Fig. 4e), revealed a pronounced new band at 535 cm^{-1} after probe conjugation, corresponding to the characteristic vibration of Au–S bonds, thus confirming the covalent nature of the probe conjugation.[54] XPS analysis provided further insight into the surface chemical state of the report probe-grafted AuNPs (Fig. 4f & Fig. S6, ESI†). An additional S signal exclusive to the report probe-grafted AuNPs was discernible in the wide-scan XPS spectra (Fig. S6, ESI†). The high-resolution S 2p spectrum of the report probe-grafted AuNPs exhibited an asymmetric and broadened peak, which was deconvoluted into two peaks at 163.4 and 164.7 eV, corresponding to the C–S and Au–S bonds, respectively (Fig. 4f).[55] This evidence proves the successful chemical bonding of the thiolated report probe onto the AuNPs.

The conjugation process of the report probes onto the AuNPs was refined by assessing the impact of the report probe

concentration and reaction duration on the grafting density of the report probes on the AuNPs (Fig. 4g and h). For reaction duration shorter than 8 h, the grafting density was positively correlated with increased reporter probe concentration, indicating an undersaturation of reporter probes on the AuNP surface. However, when the reaction duration was prolonged to 8 h or beyond, the grafting density continued to rise but reached a steady state at a report probe concentration of 0.93 ng μL^{-1}, indicating that the maximal surface capacity of the AuNPs had been saturated. Based on these observations, an optimal protocol of 0.93 ng μL^{-1} report probes and 8 h of reaction duration was implemented, which was found to achieve a grafting density of 201 report probes per AuNP, enhancing the sensitivity and detection range for *S. typhimurium* DNA. Calculations supporting these findings were provided in the ESI.†

3.3. ICP-MS analysis for the detection of *S. typhimurium*

3.3.1. Capturing *S. typhimurium* DNA by capture probe-grafted MNPs. To enhance the detection performance, we explored the effect of hybridization time and the capture probe-grafted MNP concentration on the efficiency of capturing *S. typhimurium* DNA, maintaining the DNA concentration at 10^{11} copies mL^{-1} (Fig. 5a and b). When the hybridization duration was less than 40 min, the capture efficiency gradually increased with the rising concentration of the capture probe-grafted MNPs. Upon extending the hybridization duration to over 40 min, the capture efficiency improved with increasing capture probe-grafted MNP concentration up to 1 ng μL^{-1}, beyond which a plateau was reached even when the capture probe-grafted MNP concentration was escalated to 10 ng μL^{-1}. This indicates that probe sites were almost fully occupied by the target *S. typhimurium* DNA. Consequently, a hybridization time of 40 min and a capture probe-grafted MNP concentration of 1 ng μL^{-1} were deemed as the optimal parameters, achieving a capture efficiency of 78.3% for *S. typhimurium* DNA.

3.3.2. Capturing *S. typhimurium* DNA by report probe-grafted AuNPs. For the assembly of stable sandwich-structure complexes, the efficient capture of *S. typhimurium* DNA by the report probe-grafted AuNPs is another key step. Similar to the optimization process of the hybridization of the capture probe-grafted MNPs and *S. typhimurium* DNA, the influence of hybridization time and the report probe-grafted AuNP concentration on the capture efficiency was assessed (Fig. 5c and d). The optimal conditions were identified with a report probe-grafted AuNP concentration of 2.5 ng μL^{-1} and a hybridization time of 50 min, which yielded a maximal *S. typhimurium* DNA capture efficiency of 72.8%. Therefore, we standardized the concentration of the capture probe-grafted MNPs at 1 ng μL^{-1} and the concentration of the report probe-grafted AuNPs at 2.5 ng μL^{-1}.

3.3.3. Formation and optimization of sandwich-structure complexes. The hybridization times of capture probe-grafted MNPs and report probe-grafted AuNPs to *S. typhimurium* DNA have been optimized in Sections 3.3.1 and 3.3.2, respectively (40 min and 50 min). To further optimize the incubation time for the formation of sandwich-structure complexes, 45 μL of the capture probe-grafted MNPs (1 ng μL^{-1}) and 45 μL of the report
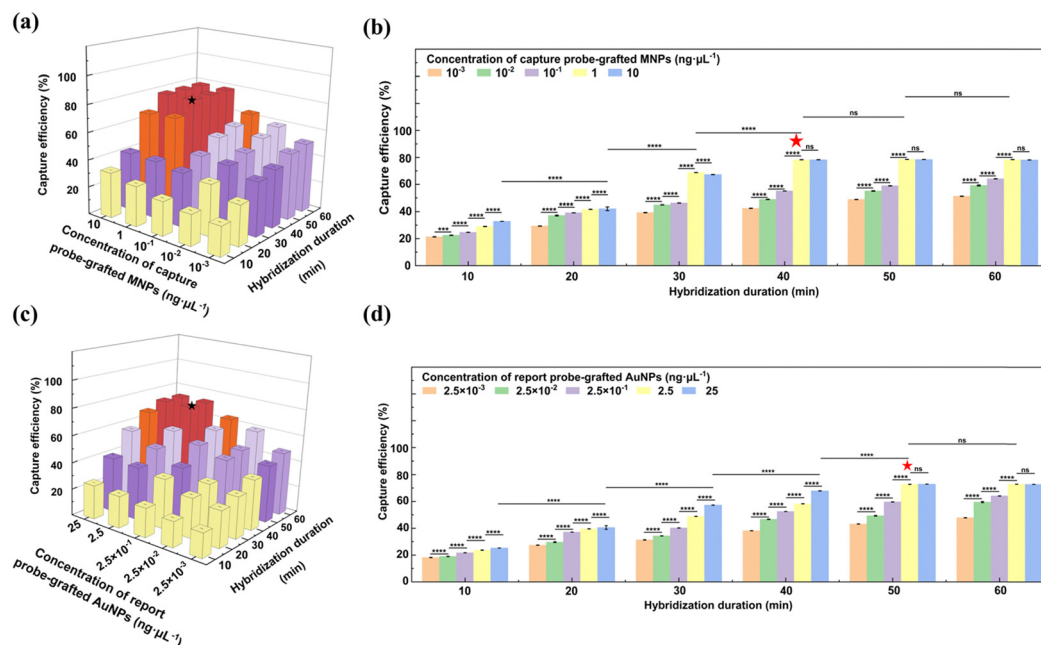
Fig. 5 Assessment of probe-grafted nanoparticles for *S. typhimurium* detection. (a) and (b) Capture efficiency of capture probe-grafted MNPs for *S. typhimurium* DNA (a), and the corresponding statistical analysis of the capture efficiency (b). (c) and (d) Capture efficiency of report probe-grafted AuNPs for *S. typhimurium* DNA (c), and the corresponding statistical analysis of the capture efficiency (d).

probe-grafted AuNPs (2.5 ng μL^{-1}) were incubated with 10 μL of *S. typhimurium* DNA (10^5 copies mL^{-1}) over 70 min at 37 °C. As shown in Fig. S8a (ESI†), a progressive increase in the capture efficiency for *S. typhimurium* DNA correlated with the increasing hybridization time. Notably, beyond 50 min, an observable plateau emerged, indicating that the maximum capture efficiency had been reached due to the saturation of available binding sites with *S. typhimurium* DNA. Thus, a 50-min hybridization duration was established as the optimal time for forming sandwich-structure complexes in the subsequent experiment.

The capture probe-grafted MNPs play a crucial role in the formation and isolation of the sandwich-structure complexes. To verify this aspect, a control experiment was designed, where 45 μL of TE buffer and 45 μL of the report probe-grafted AuNPs (2.5 ng μL^{-1}) were incubated with 10 μL of *S. typhimurium* DNA (10^5 copies mL^{-1}). The absence of the capture probe-grafted MNPs in this configuration prevented the recovery of the report probe-grafted AuNPs that bound to *S. typhimurium* DNA, resulting in a negligible detection signal (only 15.7% of that of the blank control where the capture probe-grafted MNPs were incubated with report probe-grafted AuNPs in the absence of *S. typhimurium* DNA, Fig. S7, ESI†).

To verify whether the size and number of sandwich-structure complexes affect the assay accuracy, 45 μL of different concentrations (0.25, 0.5, 1, 2, and 3 ng μL^{-1}) of the capture probe-grafted MNPs were incubated with 45 μL of the report probe-grafted AuNPs (2.5 ng μL^{-1}) and 10 μL of *S. typhimurium* DNA (10^5 copies mL^{-1}). As shown in Fig. S8b (ESI†), with increasing mass ratios of MNPs to AuNPs, there was no significant change in the detection signals as tested by ICP-MS (RSD = 0.38%).

This suggests that the size and number of the sandwich-structure complexes do not affect the assay sensitivity, given that sufficient capture probe-grafted MNPs and report probe-grafted AuNPs are present for *S. typhimurium* DNA binding.

To investigate the formation of the sandwich-structure complexes, we employed atomic force microscopy (AFM) and dynamic light scattering (DLS) for characterization. The AFM images (Fig. S8c, ESI†) confirmed the formation of the sandwich-structure complexes involving the capture probe-grafted MNPs, the report probe-grafted AuNPs, and *S. typhimurium*. Further analysis using DLS (Fig. S8d, ESI†) supports this finding, with the capture probe-grafted MNPs and report probe-grafted AuNPs displaying particle sizes of 67 ± 16 nm and 84 ± 17 nm, respectively. The addition of both types of nanoparticles in the absence of *S. typhimurium* did not result in a significant increase in the particle size but broadened the size distribution. However, upon exposure of these nanoparticles to *S. typhimurium* DNA, a primary peak at 165 ± 72 nm was observed, confirming the formation of MNPs-*S. typhimurium*-AuNPs complexes.

3.3.4. ICP-MS detection of sandwich-structure complexes. Under optimal conditions, the capture probe-grafted MNPs and report probe-grafted AuNPs formed sandwich-structure complexes with *S. typhimurium* DNA of different concentration gradients. The Au content in the sandwich-structure complexes was quantitatively analyzed by ICP-MS to quantify *S. typhimurium*. The assay showed excellent linearity ($y = 0.07787x + 0.2170$, $R^2 = 0.994$) in the range of *S. typhimurium* concentration from 10^1 to 10^{10} copies mL^{-1} (Fig. 6a). The lowest limit of detection (LOD), defined as LOD = $3\sigma/S$ (with a signal-to-noise ratio, S/N = 3, confidence level = 95%), was calculated to be 1 copy mL^{-1} based on the standard deviation (σ) of the blank. The limit of

7320 | *J. Mater. Chem. B*, 2024, **12**, 7311–7323

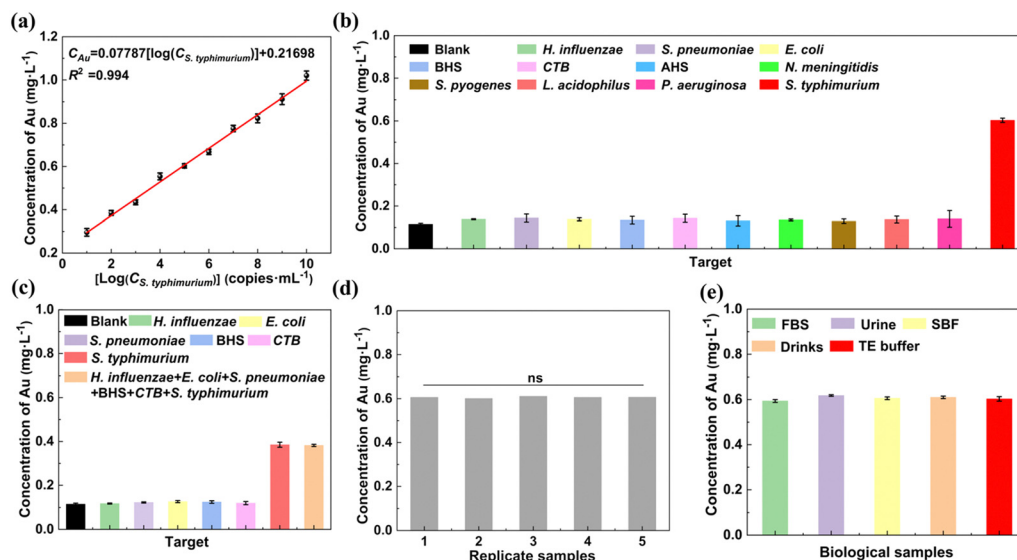This journal is © The Royal Society of Chemistry 2024

Fig. 6 (a) Correlation between the Au concentration detected by ICP-MS and the concentration of target *S. typhimurium* DNA. (b) Specificity of the method for targeting *S. typhimurium* against the interference pathogens at a uniform concentration of 10^5 copies mL^{-1}. (c) Detection performance of the method at low concentrations of *S. typhimurium* DNA (10^2 copies mL^{-1}) and high concentrations of interfering bacteria DNA (10^9 copies mL^{-1}). (d) Repeatability assay of the method. (e) Recovery of this method in biological samples.

quantification (LOQ), calculated as LOQ = $10\sigma/S$ (S/N = 3, confidence level = 95%), was 2 copies mL^{-1}, based on the 10σ value of the blank (*S. typhimurium* is a haploid bacterium, containing only one copy of DNA in each bacterial cell). To evaluate the specificity of the sandwich hybridization strategy for detecting *S. typhimurium*, we tested 10 other pathogenic bacteria that may interfere with the *S. typhimurium* detection process. The DNA concentrations of both the *S. typhimurium* target and these interference pathogens were standardized to 10^5 copies mL^{-1}. The target *S. typhimurium* had a significantly stronger signal compared to the interference pathogens, which yielded responses comparable to the blank group. Specifically, the responses from the interference pathogens were ≤ 6% of the target signal (Fig. 6b). To further validate the specificity of our detection strategy, we performed anti-interference tests by introducing a low concentration of *S. typhimurium* DNA

(10^2 copies mL^{-1}) into samples containing a high concentration (10^9 copies mL^{-1}) of DNA from potential interfering bacteria: *H. influenzae*, *S. pneumoniae*, *E. coli*, BHS, or CTB. As shown in Fig. 6c, the presence of the high concentration of interfering bacterial DNA did not generate any significantly different detection signals compared to the blank group which lacked bacterial DNA. To further evaluate cross-reactivity, we mixed the low concentration of *S. typhimurium* DNA with all the high concentrations of the aforementioned interfering bacterial DNAs. The results confirmed that the presence of high concentrations of interfering bacterial DNAs did not impact the detection accuracy.

To assess the repeatability of our detection system, five samples, each containing 10^5 copies mL^{-1} of *S. typhimurium* DNA, were analyzed. The resulting signals were highly consistent across all samples (Fig. 6d), confirming the good repeatability.

Table 1 Recovery of *S. typhimurium* by this method in biological samples

Biological samples	Added *Salmonella typhimurium* (log$_{10}$ CFU mL^{-1})	Detected *Salmonella typhimurium* (log$_{10}$ CFU mL^{-1})	Recovery (%)	RSD (%, n = 3)
FBS	5	4.74	96.8	1.61
		4.93		
		4.88		
Urine	5	5.18	102.8	0.90
		5.09		
		5.19		
SBF	5	4.96	99.2	1.54
		5.10		
		4.92		
Mizone® Drink	5	4.97	101.0	1.43
		5.02		
		5.14		
TE buffer	5	4.94	100.0	0.75
		5.00		
		5.03		

To evaluate the potential application, *S. typhimurium* DNA in biological samples such as FBS, urine, SBF, Mizone® drink, and TE buffer was detected, respectively. The results in Fig. 6e and Table 1 indicate that our strategy yielded recovery of 96.8% to 102.8%, with RSDs ranging from 0.75% to 1.61% across all tested biological samples. Comparative analysis with existing detection protocols for *S. typhimurium* DNA (Table S3, ESI†), revealed that both the recovery and RSDs achieved with our assay were superior to previously reported methods.

Moreover, our method outperforms previously reported methods for detecting *S. typhimurium*, as shown in Table S3 (ESI†). It achieves a broader linear detection and an outstanding low LOD. Such excellent performance can be largely attributed to the popcorn-shaped AuNPs and the clustered MNP. These structures provide a high specific surface area which facilitates rapid and stable conjugation of a large number of oligonucleotide probes, thereby enhancing the capture efficiency of *S. typhimurium*.

4. Conclusion

We have successfully engineered MNPs and AuNPs of unique morphology, followed by functionalizing with selective probes to bind with *S. typhimurium* DNA. Special sandwich-structured complexes were formed during the detection. The MNPs confer the benefit of easy magnetic separation of the composites, and the subsequent ICP-MS analysis of Au element results in a substantial amplification of detection signals. Thus, the accuracy and sensitivity were simultaneously improved, offering a straightforward and rapid operational protocol for pathogen detection.

Author contributions

Yujie Zhou: investigation, data curation, formal analysis, writing – original draft; Zhihui Tang: investigation, data curation, formal analysis, writing – review & editing; Lei Li: investigation, formal analysis, validation, writing – original draft; Yuzuo Chen: investigation, formal analysis; Yuanyuan Xu: investigation, formal analysis; Renjie Liu: investigation, formal analysis; Yanrong Zhang: investigation, formal analysis; Xiaoyan Liu: resources, supervision; Wenjuan Yang: resources, supervision; Baoning Wang: conceptualization, resources, supervision; Jieyu Zhang: conceptualization, resources, supervision, writing – review & editing; Qing Jiang: conceptualization, resources, supervision, writing – review & editing; Yunbing Wang: conceptualization, resources, supervision.

Data availability

The data supporting this article have been included within the article and the ESI.†

Conflicts of interest

There are no conflicts to declare.

Acknowledgements

References

1 A. Prasad, S. Khan, J. K. Monteiro, J. Li, F. Arshad, L. Ladouceur, L. Tian, A. Shakeri, C. D. M. Filipe, Y. Li and T. F. Didar, *Adv. Mater.*, 2023, **35**, 2302641.

2 S. Wei, Z. Su, X. Bu, X. Shi, B. Pang, L. Zhang, J. Li and C. Zhao, *npj Sci. Food*, 2022, **6**, 48.

3 J. Li, S. Khan, J. Gu, C. D. M. Filipe, T. F. Didar and Y. Li, *Angew. Chem., Int. Ed.*, 2023, **62**, e202300828.

4 L. Chui, C. Ferrato, V. Li and S. Christianson, *Microorganisms*, 2021, **9**, 955.

5 M. G. Aruta, E. Lari, D. De Simone, B. Semplici, C. Semplici, H. Dale, E. Chirwa, I. Kadwala, M. Mbewe, H. Banda, M. Iturriza-Gomara, M. Gordon, T. Nyirenda, P. Piu, M. Pizza, F. Berlanda Scorza, S. Grappi, R. Canals, O. Rossi and B. O. T. V. On, *Biotech*, 2023, **12**, 54.

6 M. Arnold, R. P. Smith, F. Martelli and R. Davies, *Zoonoses Public Health*, 2024, **00**, 1–12.

7 Y. Ding, Z. Li, C. Huang, Y. Zhang, J. Wang and X. Wang, *J. Food Saf.*, 2023, **43**, e13091.

8 R. Heymans, A. Vila, C. A. M. van Heerwaarden, C. C. C. Jansen, G. A. A. Castelijn, M. van der Voort and E. G. Biesta-Peters, *PLoS One*, 2018, **13**, e0206316.

9 J. Gao, Y. Jiao, J. Zhou and H. Zhang, *Talanta*, 2024, **270** 125553.

10 E. Kim, S. Yang and H. Kim, *Food Biosci.*, 2023, **56**, 103242.

11 K. G. Maciorowski, P. Herrera, F. T. Jones, S. D. Pillai and S. C. Ricke, *Vet. Res. Commun.*, 2006, **30**, 127–137.

12 H. Ahari, S. Kakoolaki and S. A. A. Anvar, *Int. J. Environ. Sci. Technol.*, 2017, **14**, 2149–2154.

13 J. G. Bruno, *J. Microbiol. Methods*, 2022, **193**, 106406.

14 Z. Guan, Y. Sun, C. Ma, J. J. Lee, S. Zhang, X. Zhang, Z. Guo and Y. Du, *Biosens. Bioelectron.*, 2023, **236**, 115438.

15 J. Zhao, M. Han, A. Ma, F. Jiang, R. Chen, Y. Dong, X. Wang, S. Ruan and Y. Chen, *J. Hazard. Mater.*, 2024, **466**, 133648.

16 H. Li, H. Xu, S. Yao, S. Wei, X. Shi, C. Zhao, J. Li and J. Wang, *Talanta*, 2024, **270**, 125505.

17 F. Zhao, H. Yan, Y. Zheng, Y. Zu, S. Yang, H. Hu, S. Shi, H. Liang and X. Niu, *Food Chem.*, 2023, **426**, 136581.

18 L. Li, Q. Li, Z. Liao, Y. Sun, Q. Cheng, Y. Song, E. Song and W. Tan, *Anal. Chem.*, 2018, **90**, 9621–9628.

19 J. Ren, G. Liang, Y. Man, A. Li, X. Jin, Q. Liu and L. Pan, *PLoS One*, 2019, **14**, e0218325.

7322 | *J. Mater. Chem. B*, 2024, **12**, 7311–7323

This journal is © The Royal Society of Chemistry 2024

20 D. Vijian, S. V. Chinni, L. S. Yin, B. Lertanantawong and W. Surareungchai, *Biosens. Bioelectron.*, 2016, **77**, 805–811.

21 P. Murasova, A. Kovarova, J. Kasparova, I. Brozkova, A. Hamiot, J. Pekarkova, B. Dupuy, J. Drbohlavova, Z. Bilkova and L. Korecka, *J. Electroanal. Chem.*, 2020, **863**, 114051.

22 Y. Zhang, F. Ren, G. Wang, T. Liao, Y. Hao and H. Zhang, *Sens. Actuators, B*, 2021, **329**, 129273.

23 S. Tu, M. Golden, W. F. Fett, A. Gehring and P. Irwin, *J. Food Saf.*, 2003, **23**, 75–89.

24 B. Meermann and V. Nischwitz, *J. Anal. At. Spectrom.*, 2018, **33**, 1432–1468.

25 X. Wang, W. Chen, H. Yang, X. Zhang, M. Deng, X. Zhou, K. Huang, P. Chen and B. Ying, *Microchim. Acta*, 2020, **187**, 453.

26 X. Huang, Z. Zhang, L. Chen, Y. Lin, R. Zeng, J. Xu, S. Chen, J. Zhang, H. Cai, H. Zhou and P. Sun, *Biosens. Bioelectron.*, 2022, **212**, 114414.

27 S. Yao, B. Pang, Y. Fu, X. Song, K. Xu, J. Li, J. Wang and C. Zhao, *Sens. Actuators, B*, 2022, **359**, 131581.

28 X. Xu, J. Chen, B. Li, L. Tang and J. Jiang, *Analyst*, 2019, **144**, 1725–1730.

29 Y. Lin and A. T. Hamme II, *J. Mater. Chem. B*, 2015, **3**, 3573–3582.

30 W. Xiuji, J. Lanlan, G. Wei, H. Liuqin and S. H. And, *At. Spectrosc.*, 2017, **38**, 44–50.

31 S. Crestani, A. Leitolis, L. F. O. Lima, M. A. Krieger and L. Foti, *J. Immunol. Methods*, 2016, **435**, 17–26.

32 N. Sun, Y. Ding, Z. Tao, H. You, X. Hua and M. Wang, *Food Chem.*, 2018, **257**, 289–294.

33 K. Kang and H. Jang, *Bull. Korean Chem. Soc.*, 2016, **37**, 1391–1392.

34 T. Chen, Q. Chu, M. Li, G. Han and X. Li, *J. Nanobiotechnol.*, 2021, **19**, 206.

35 Q. Xu, X. Guo, L. Xu, Y. Ying, Y. Wu, Y. Wen and H. Yang, *Sens. Actuators, B*, 2017, **241**, 1008–1013.

36 S. Xuan, F. Wang, Y. J. Wang, J. C. Yu and K. C. Leung, *J. Mater. Chem.*, 2010, **20**, 5086–5094.

37 M. Esmaeilpour, A. R. Sardarian and J. Javidi, *Appl. Catal.*, 2012, **445–446**, 359–367.

38 N. Xu, H. Yan, X. Jiao, L. Jiang, R. Zhang, J. Wang, Z. Liu, Z. Liu, Y. Gu, F. Gang, X. Wang, L. Zhao and X. Sun, *J. Cryst. Growth*, 2020, **547**, 125780.

39 T. Jesionowski, F. Ciesielczyk and A. Krysztafkiewicz, *Mater. Chem. Phys.*, 2010, **119**, 65–74.

40 S. Xuan, L. Hao, W. Jiang, X. Gong, Y. Hu and Z. Chen, *J. Magn. Magn. Mater.*, 2007, **308**, 210–213.

41 Y. Zhang, S. Wang, S. Shen and B. Zhao, *Chem. Eng. J.*, 2013, **233**, 258–264.

42 D. Li, W. Y. Teoh, J. J. Gooding, C. Selomulya and R. Amal, *Adv. Funct. Mater.*, 2010, **20**, 1767–1777.

43 Y. Liu, W. Luo, Q. Fan, H. Ma, Y. Yin and J. Guan, *Adv. Funct. Mater.*, 2023, **33**, 2303470.

44 D. Wan, G. Wang, W. Li and X. Wei, *Appl. Surf. Sci.*, 2017, **413**, 398–407.

45 Y. Dang, G. Wang, G. Su, Z. Lu, Y. Wang, T. Liu, X. Pu, X. Wang, C. Wu, C. Song, Q. Zhao, H. Rao and M. Sun, *ACS Nano*, 2022, **16**, 4536–4550.

46 R. De Palma, S. Peeters, M. J. Van Bael, H. Van den Rul, K. Bonroy, W. Laureyn, J. Mullens, G. Borghs and G. Maes, *Chem. Mater.*, 2007, **19**, 1821–1831.

47 M. C. Stuparu and A. Khan, *J. Polym. Sci., Part A: Polym. Chem.*, 2016, **54**, 3057–3070.

48 L. Wu, S. Zhou, Y. Yun, L. Zhu, B. Li and W. Zhang, *Sens. Actuators, B*, 2022, **356**, 131124.

49 Q. Sun, X. Ma, Y. Lu, S. Wang and H. Zhong, *Powder Technol.*, 2021, **380**, 421–429.

50 X. Liu, S. Zhang, Z. Cheng, X. Wei, T. Yang, Y. Yu, M. Chen and J. Wang, *Anal. Chem.*, 2018, **90**, 12116–12122.

51 Y. Zhang, T. Wu, Q. Cui, Z. Qu, Y. Zhang, H. Ma and Q. Wei, *Biosens. Bioelectron.*, 2023, **222**, 114992.

52 S. A. Sufyan, B. van Devener, P. Perez and M. M. Nigra, *ACS Appl. Mater. Interfaces*, 2023, **15**, 1210–1218.

53 Y. Xing, J. Han, X. Wu, D. T. Pierce and J. X. Zhao, *Microchim. Acta*, 2019, **187**, 56.

54 Y. Negishi, K. Nobusada and T. Tsukuda, *J. Am. Chem. Soc.*, 2005, **127**, 5261–5270.

55 J. Xing, Z. Xu and B. Deng, *Polymers*, 2018, **10**, 83.

This journal is © The Royal Society of Chemistry 2024

J. Mater. Chem. B, 2024, **12**, 7311–7323 | **7323**